Geometry-driven asymmetric cell divisions pattern cell cycles and zygotic genome activation in the zebrafish embryo

Nikhil Mishra, Yuting I. Li, Edouard Hannezo, and Carl-Philipp Heisenberg*
Institute of Science and Technology Austria, Klosterneuburg, Austria
*e-mail: heisenberg@ista.ac.at

Abstract

Synchrony in early embryonic cell cycles, followed by gradual desynchronization at the midblastula transition (MBT), is a widely conserved feature across animal phylogeny. Embryos that fail to maintain synchrony during these early stages do not develop properly, highlighting the critical importance of this process. However, the mechanisms underlying the initial synchronization and subsequent desynchronization of cell cycles - and their developmental significance - remain poorly understood. Here we show that the initial cell cycles in zebrafish embryos are synchronized primarily through cell-autonomous mechanisms. Furthermore, we reveal that their gradual desynchronization is spatially patterned by the geometry of the dividing embryo, which establishes a cell volume gradient through unequal cell divisions. This volume gradient translates into a cell cycle gradient by unequal S-phase lengthening due to volume-dependent changes in the nucleocytoplasmic ratio. Importantly, we find that this volume gradient, and the resulting cell cycle gradient, also spatiotemporally patterns the initiation of zygotic genome activation (ZGA) - a hallmark of MBT - within the embryo, thereby serving as a key symmetry-breaking event in animal development. Thus, our findings uncover a previously unrecognized role for early embryonic geometry in establishing an axis of transcriptional asymmetry during the transition to developmental autonomy.

Main

Cell cycles in the zebrafish embryo are synchronized in a cell-autonomous manner

Metazoan development begins with a single cell, the zygote, which undergoes several rounds of rapid divisions (cleavages) to generate a large population of cells capable of adopting multiple fates and exhibiting diverse morphogenetic behaviors. In many invertebrate and vertebrate species, these early divisions are initially highly synchronous. This cell cycle synchrony is best understood in *Drosophila*, where it is driven by the propagation of a chemical wave. In cleavage-stage *Drosophila* embryos, which are syncytial, nuclear cycles synchronize through "sweep waves"- a combination of coupling-dependent trigger waves and coupling-independent phase waves of Cyclin-dependent kinase 1 (Cdk1) activity propagating through the cytoplasm[1]. Similar mechanisms have been observed in *Xenopus* egg extracts, another syncytial system, where nuclear divisions are coordinated by trigger waves of Cdk1 activity[2]. By contrast, in intact *Xenopus* embryos, where cells are fully separated, early cleavage divisions synchronize independently of cell-cell coupling[3]. Notably, across systems, the propagation of cell cycle waves slows progressively with successive cleavage rounds, leading to 'metasynchronization', where cell cycles remain spatially patterned before eventually becoming fully desynchronized[1,3,4].

Although conserved across diverse species, the mechanistic basis for cell cycle meta- and desynchronization is only poorly understood. Notably, the loss of cell cycle synchrony often coincides with the midblastula transition (MBT), a stage characterized by zygotic genome activation (ZGA) and the initiation of morphogenetic movements[3,5,6]. This correlation suggests functional links between these processes. Previous studies have proposed that ZGA is triggered by developmental timing and the maturation of cellular components, such as the nuclear pore complex[7]. Additionally, factors like the counting of cell cycles, lengthening of the cell cycle to allow more time for transcription, and the titration of transcriptional repressors - achieved through a reduction in the relative size of the nucleus to the cytoplasm (nucleocytoplasmic ratio) during reductive cell divisions - have been implicated[8–12]. Yet, whether and how these factors are linked to cell cycle synchronization and how ZGA is not only temporally but also spatially regulated within the early embryo, remains unclear.

Initial cleavages in the zebrafish embryo are meroblastic; i.e. the cytoplasm but not the yolk is partitioned through cytokinesis[4]. Cell cycles at this stage occur highly synchronously, to begin with, and gradually desynchronize (metasynchrony) before completely desynchronizing at division round 10[4]. Importantly, while the cleavage-stage cells cycle between only the S and M phases, complete desynchronization at division round 10 is thought to occur mainly due to a heterogeneous introduction of gap phases to the cell cycles[13]. To determine the spatiotemporal pattern of cell divisions in cleavage-stage zebrafish embryos, we recorded time-lapse images of Tg*(actb2:rfp-pcna)* embryos, allowing us to reliably score the onset of mitosis[14]. Consistent with previous reports, we observed three distinct phases with different extents of mitotic synchrony[4,5]. In the first three cell cleavage division rounds, cell cycles exhibited very high synchrony (**synchronous phase**) (Fig. 1B, S1A-B). Thereafter, cell divisions from cleavage rounds four to nine showed slight but clearly detectable delays (**metasynchronous phase**) (Fig. 1B, S1A-B). These delays increased throughout the metasynchronous phase, with cells in division round four dividing with a mean division timing variance of 0.10 min^2 and in division round 9 with 3.43 min^2 (Fig. 1B). Notably, as previously reported, these metasynchronous divisions occurred in a spatiotemporally patterned manner, forming a radial 'mitotic wave' that originates near the animal pole (AP), where cells divide first, and

propagates toward the margin, where they divide last (Fig. 1C, S1C-D)[4,15,16]. Furthermore, consistent with the increasing variance in division timings during the metasynchronous phase, the speed at which this mitotic wave travels gradually decreased over consecutive division rounds (Fig. 1D). After round nine, cells divided largely non-synchronously, marking the onset of the **asynchronous phase**.

To understand how cell cycles are seemingly coordinated into radial mitotic waves during the metasynchronous phase, we asked whether neighboring cells within the embryo can synchronize their cell division cycles. We found that neighboring cells that originated from a common cell division (sister cells) were significantly more synchronized than those not originating from the same cell division (non-sister cells) (Fig. 1E). This suggests that cell lineage, rather than cell-cell proximity, affects cell division timing such that cells closely related by lineage likely inherit more synchronized internal 'clocks' than those inherited by unrelated cells. To further challenge this possibility, we artificially desynchronized cell cycles at the 32/64-cell stage through mosaic Histone 1 protein injections, previously been shown to effectively alter cell cycle progression[17–19]. We found that Histone 1-positive and thus desynchronized cells failed to resynchronize with their neighboring control cells by division round 9, after which cell cycles normally desynchronize in control embryos (Fig. 1F, S2, Movie S2). To address the possibility that these cell cycles could have resynchronized given sufficient time, we assessed cell cycle progression in embryos ectopically expressing the Cdk1 inhibitor, Chek1, through *chek1* mRNA injection in the one-celled embryo, which, by being heterogeneously distributed in the embryo, has previously been shown to interfere with cell cycle synchronization[20]. Chek1-overexpressing embryos exhibited cell cycle desynchronization significantly earlier than control embryos, and failed to resynchronize despite completing all cleavage division rounds (Fig. 1G, S2, Movie S3). These observations suggest that cell-cell coupling through mechanisms other than cell lineage plays only a minor role, if any, in cell cycle synchronization in the zebrafish embryo.

The transition from synchrony to metasynchrony was gradual rather than abrupt, suggesting a progressive accumulation of delays rather than distinct switches leading to the observed loss of synchrony (Fig. 1B). Importantly, this gradual loss of synchrony was due to unequal cell cycle periods. For instance, between the metasynchronous division rounds 6-8, cells at the margin cycled with 2-4% longer periods than those at the AP. This discrepancy arose exclusively due to a longer S-phase, which increased in cells as a function of their distance from the animal pole (Fig. 1H-I). Such period gradients might lead to the observed gradual slowing down of the radial mitotic wave by accumulating increasing delays in the marginal cells over consecutive division rounds. To test this hypothesis, we assumed that the period, T, is a linear function of the distance 'z' from the AP where $T = T_0(1 + \frac{kz}{L})$, with T_0 being the typical period at the AP, L the total AP-margin distance, and k a dimensionless constant of proportionality. This implies that the speed of the mitotic wave, v, in the nth division round is expected to be inversely proportional to n (Fig. 1D) with $v = \frac{L}{T_0}\frac{1}{kn}$. To compare our experimental observations with these theoretical predictions, we first performed linear regression on the division timings to obtain the wave speed for each division round (Fig. S1D). We then fitted the obtained v against $\frac{1}{n}$ using the least square fit. Using $k=1.9\%$, we obtained a close match between experiments and theory (Fig. 1D), suggesting that a 1.9% slower cell cycle at the margin would, in principle, be sufficient to explain the observed slowing down of the mitotic waves during consecutive division rounds. Considering that we experimentally observed a 2-4% longer period at the margin, close to the theoretically predicted 1.9%, this suggests that a linear gradient

of cell cycle periods, rather than cell-cell coupling, gives rise to the observed radial mitotic waves found during embryonic cleavages.

Increased cell-cell coupling reshapes the mitotic wave and prevents desynchronization

Next, to verify our conclusion that the mitotic waves are produced in a coupling-independent manner, we asked how they would appear if the cell cycles were instead coupled. To that end, we performed numerical simulations of the Kuramoto model of interacting oscillators on a hemisphere with free boundary conditions[21] (Fig. 2A). The oscillators were placed on a Fibonacci lattice covering the hemisphere, with nearest neighbors obtained with Delaunay triangulation. The phases of the oscillators obeyed the following equation: $\delta_t\theta_i = \omega_i + \epsilon \sum_{j\in N_i} sin(\theta_j - \theta_i)$ where ω_i represents the natural frequency of the *i*-th oscillator, and the second term describes the interactions between neighboring oscillators parametrized by the interaction strength ϵ, with N_i being the nearest neighbors of the *i*-th oscillator. Due to cell-to-cell variations, we further assumed the presence of noise in the cell cycle lengths. Mathematically, we decomposed the frequencies into two parts $\omega_i = \varpi(z) + \Lambda_i$, where the first term $\varpi(z)$, is the inherent AP-to-margin oscillation gradient, and the second term is an independent spatial noise with covariance $\langle \Lambda_i \Lambda_j \rangle = \sigma\delta_{ij}$. Simulations with small interaction strength (ϵ) and low noise (σ) recapitulated the wild-type behavior, where mitotic waves originated at the AP, and accumulated delays causing a gradual slow-down over time (Fig. 2B-C). In contrast, the introduction of greater interaction strength and noise led the system to self-organize into smooth mitotic waves originating at the margin, similar to the case in *Xenopus* egg extracts, even though the 'natural' cell cycle lengths at the AP were preset to be shorter on average[22] (Fig. 2B, D). For even larger values of noise, multiple waves emerged from random points of the simulated embryo (Fig. 2B). Overall, this theoretical phase diagram suggests that wild-type embryos are characterized by low to intermediate noise and very little coupling and that increasing cell coupling should, in theory, shift the origin of the mitotic wave from the AP to the blastoderm margin.

To experimentally test this prediction, we syncytialized cleavage-stage embryos by preventing cytokinesis but not karyokinesis through transient Aurora Kinase B inactivation[23] (Fig. 2E-F). We reasoned that a syncytialized embryo would mimic the situation in *Drosophila* embryos and *Xenopus* egg extracts, both syncytial systems, where cell cycles are synchronized partially or completely through coupling-dependent trigger waves and would, therefore, comprise a coupled system. Remarkably, we found, consistent with our theoretical predictions, that in syncytial embryos, the mitotic wave originated at the margin rather than at the AP, as it does in control embryos (Fig. 2B, D, F Movies S1, S4). Comparing the wave characteristic at the 8th round of divisions allowed us to estimate the effective coupling to noise ratio in syncytial embryos (Fig. 2G). Interestingly, when examining not just the overall origin of the waves but also the quantitative changes in synchronization over time (quantified by division time variance for different division rounds) predicted another key difference in the model between intact and syncytial embryos. Indeed, in the absence of coupling (intact embryo), noise should gradually accumulate, leading to monotonously increasing timing variance, whereas, with coupling (syncytial embryo), the variance should plateau over time with a characteristic time scale dependent on the exact value of the coupling parameter (Fig. 2H). Strikingly, this was confirmed in our experiments: in syncytial embryos (unlike in controls), 'cells' continued to cycle metasynchronously even beyond the 10th division round, indicating tight coupling between cell cycles (Fig. S3A, Movies S1, S4), with the evolution of the variance well-described by our theoretical prediction (for ϵ=0.08 and σ=0.028 Fig. 2H). For intact embryos, the variance continuously increases, although with an even faster temporal scaling than in the model

for later cleavages (Fig. 2I). Interestingly, considering the fact that cytokinesis is incomplete at early cleavages (i.e. that couplings initially exist but rapidly decay to near zero for later cleavages) could explain quantitatively the experimental data for intact embryos (see SI Theory Note for more details on the approach and assumptions)[24].

Finally, to further challenge the increased coupling of syncytial 'cells', we injected *chek1* mRNA into embryos before syncytialization and assessed whether they could resist premature desynchronization typically caused *by chek1* expression in intact wild-type embryos (Figs. 1G, S1, Movie S3). Indeed, we reasoned theoretically that the values of couplings inferred for syncytial embryos were large enough that they should be able to override a significant increase in noise, such as the desynchronizing effects of *chek1* expression (Fig. 2B). Indeed, we found that in *chek1*-expressing embryos, the mitotic waves originated at the margin, and 'cells' continued to cycle metasynchronously even beyond the 10th division round, suggesting that cells in the syncytial embryo are, in fact, tightly coupled. (Fig. S3B-C, Movie S5). By extension, this implies that such a coupling is absent/minimal in intact embryos and, consequently, that mitotic waves are produced largely independently of cell-cell interactions in wild-type embryos. Collectively, these findings suggest that cell cycles are only weakly coupled during cleavages and that metasynchrony arises predominantly by cell-autonomous processes.

Early embryo geometry establishes a cell volume gradient along the AP-margin axis through guided asymmetric cell divisions

For the cell cycle to slow down from the AP to the margin in a predominantly cell-autonomous manner, there must be a factor causing unequal lengthening of the S-phase along the AP-margin axis. Among the most important factors regulating S-phase length is the nucleocytoplasmic (N/C) ratio[25,26]. A high N/C ratio causes S-phase lengthening, for instance, by retarding Cdk1 activation[25]. Consistent with such an effect of the N/C ratio on cell cycle length, we found that the length of the S-phase across the metasynchronous cleavage rounds negatively correlated with cell volume (Fig. S4A-B). Therefore, we hypothesized that an AP-margin gradient of cell volumes in the cleavage-stage embryo might be responsible for unequally slowing down the cell cycle length from the AP to the margin. To test this hypothesis, we measured cell volumes by semi-automatically segmenting surface cells at the 128-cell stage (round 8). Indeed, we found that, on average, cells closer to the AP were significantly larger than those away from it (Figs. 3A, S4G). To determine at what stage such a volume gradient first becomes apparent, we also measured cell volumes in embryos at the 8-cell stage (round 4) and the 16-cell stage (round 5) - the first stages where cells can be classified as being 'central' or 'peripheral' based on their position. Interestingly, we observed that cells closer to the AP were consistently larger than the marginal cells at both these stages, showing that the AP-margin gradient of cell volumes arises already in the very early embryo (Fig. 3B, C). However, no such gradient was observed for the nuclear volume, indicating that the peripheral cells have a larger N/C ratio (Fig. 3B). Furthermore, the cell volume gradient not only persisted but was also further enhanced by subsequent cell divisions, as mother cells having unequal sizes themselves again divided asymmetrically to produce yet unequally sized daughters, thereby further diversifying cell volumes through cell lineage in addition to the already established position-driven cell volume diversity (Fig. 3D). For such unequal cell divisions to robustly give rise to a gradient in cell volumes along the AP-margin axis, upon division the daughter cell closer to the AP must be on average bigger than the daughter cell further from the AP. In line with this, we found that cell divisions in the early cleavage stages showed a tendency to produce larger daughter cells closer to AP, with the central daughter cell (closer to AP) being, on average, ~12.4% larger by volume than its peripheral sister cell (away from AP) (Fig. 3E).

To determine what causes such patterned asymmetric cell divisions, we investigated how cell divisions are oriented and the cleavage plane positioned in the early embryo. While several sophisticated models have been proposed to explain the orientation and positioning of the cleavage plane across systems, we started by first testing if following the simplest model, the ~140-year old Hertwig's rule, can recapitulate the experimentally observed pattern of asymmetry[27,28]. More specifically, we assumed that the mitotic spindle in dividing blastomeres would orient along the longest cell axis, thereby dividing the cell along this axis. To test if such a geometry-driven mechanism would suffice to generate the observed pattern of asymmetric cell divisions and, therefore, the cell volume gradient, we predicted daughter cell volumes at the 16-cell stage by first identifying the longest axes of segmented cells at the 8-cell stage through Principal Component Analysis and then bisecting them to obtain two daughter cells from each division[29] (Fig. 3E). Indeed, we found that with this approach, the predicted daughter cell size asymmetry closely matched the observed asymmetry for most cell divisions, such that the central daughter cells (closer to the AP) at the 16-cell stage were, on average, ~18.5% larger than their peripheral sister cells (further away from the AP) by volume (Fig. 3E). Importantly, this tendency of central daughter cells being bigger than peripheral ones is determined by the specific geometry of the first cell of the fertilized egg, the blastodisc, that is delineated not only by a plasma membrane at its outer side, but also by the interface to the yolk granules on its inner side[4,30]. As the interface to the yolk granules is curved, the first cell division will give rise to equally sized daughter cells that are more pointed and narrow at their peripheral ends. Dividing these cells again along the same axis will then, as a result, generate daughter cells where the central cell is larger than the peripheral one. This suggests that a gradient of cell volumes along the AP-margin axis in the cleaving embryo can be explained by the specific geometry of the first cell in the fertilized egg leading to unequal cell division along the AP-margin axis during subsequent division rounds.

Cell volume gradient causes patterned cell cycle lengthening along the AP-margin axis

Whereas the influence of cell volume on cell cycle length is established in several systems, such a relationship in zebrafish embryos is still unclear, owing to contradicting reports as to the determinative role of cell size in this context[5,16]. Therefore, to unequivocally establish the role of cell volume, and consequently the N/C ratio, in determining cell cycle lengths, we first increased the N/C ratio at the one-cell stage by aspirating cytoplasm from the blastodisc (Fig. S4C). Consistent with the role of high N/C ratios in prolonging cell cycles, we observed that in different embryos, the S-phase lengthened prematurely or significantly more, and cell cycles desynchronized earlier than in control embryos (Fig. S4D). Reversely, we decreased the N/C ratio by replicating an experiment by Kane and Kimmel[4], where we aspirated one nucleus from two (or four)-cell stage embryos (Fig. S4E). In such embryos, only the control half initially underwent cleavages, while no cleavages occurred in the other, enucleated half (Fig. S4E, Movie S6). However, in a subset of the embryos at the 4th or 5th division round, nuclei from the control half invaded the enucleated half, which then commenced cleavages (Fig. S4E, Movie S6). Notably, despite all nuclei at this stage having undergone the same number of cycles, those in the previously enucleated half now resided in a much larger volume of cytoplasm and, consequently, displayed a smaller N/C ratio. In line with previous findings, these nuclei displayed delayed S-phase lengthening and continued to cycle metasynchronously beyond the 10th division round, the stage when cell cycles in the 'control' half typically desynchronize[5] (Fig. S4F).

Having confirmed that the N/C ratio, in principle, can influence the S-phase length, we asked how perturbing the embryo-scale cell volume gradient within the cleaving embryo would affect cell cycle

(meta)synchrony and, consequently, the mitotic wave. To alter the cell volume gradient, we first generated bi-lobed embryos displaying two ectopic 'animal poles' by mounting two-cell stage embryos in low melting point agarose (0.67% w/v in E3 buffer) when the first cytokinesis was in progress (Fig. 4A). We reasoned that spatially confining and, therefore, reshaping the embryo in this manner would produce larger cells away from the AP at the two ectopic (morphological) animal poles. Interestingly, we found that not only the gradient of cell volumes was reshaped in the embryo, but also that two mitotic waves, one from each of the two ectopic APs, supporting the notion that the cell volume gradient is linked to the emergence of the mitotic wave (Fig. 4A, B, Movie S7). To further challenge this suggestion, we removed a part of the yolk on the vegetal side of the two-cell stage embryo to increase the curvature of the blastodisc (the two blastomeres positioned on the yolk cell; Fig. 4C). Based on our analysis indicating that the cell volume gradient is a product of the curvature of the blastodisc-yolk interface, we reasoned that this increased curvature would reorient the longest axes of the two cells, such that they align more along the animal-vegetal (AV) axis, which would then amplify the volume asymmetry of cleavage divisions and, consequently, the phase difference between cell cycles (Fig. 4C). Strikingly, we found that in yolk-severed embryos with cell divisions more aligned along the AV axis, the mitotic wave indeed showed a greater cell division timing variance compared to the control embryos (Fig. 4C-D, Movie S8). Taken together, these observations strongly support the notion that a gradient of cell volume along the AP-margin axis, guided by embryo geometry, causes the generation of a gradient of S-phase lengths along the AP-margin axis of the blastoderm, thereby generating radial mitotic waves in the zebrafish embryo.

Among the major responders to a high N/C ratio is Chek1, which, when active, delays the S-M transition[25]. Therefore, having determined that a gradient of cell volumes patterns cell cycle lengths in the zebrafish embryo, we inquired whether Chek1 mediates the effect of cell volume on S-phase length. To that end, we inhibited Chek1 activity by treating embryos with 10 µM PF477736, a specific Chek1 activity inhibitor[31]. If Chek1 activity is required for the gradual metasynchronization of cell cycles through unequal S-phase lengthening, the cell cycle progression would be expected to show less variations in the treated embryos. Consistent with this, we found that, while Chek1-inhibited embryos produced mitotic waves like those in control embryos, they indeed exhibited a lower mitotic division timing variance (Fig. 4E, Movie S9). This suggests that Chek1 activity is critical for translating a cell volume gradient into a mitotic wave along the AP-margin axis of the blastoderm.

Cell volume/cell cycle period gradients pattern ZGA along the AP-margin axis

Finally, we asked if the geometry-driven cell volume gradient and the resulting patterned mitotic metasynchrony play a developmental role that may impact embryogenesis beyond the cleavage stages. Mitotic metasynchrony in zebrafish embryos diminishes concomitantly with the onset of ZGA, which sets up the blueprint for cell fate heterogeneity, a process central to metazoan development[5]. Therefore, considering the previously reported roles of cell volume and cell cycle length on ZGA, we asked if the onset of zygotic transcription is influenced by the observed cell volume gradient and resulting mitotic metasynchrony[10]. To this end, we assessed when and where zygotic transcription is initiated in the embryo by performing native pri-*miR430* transcription imaging through MOrpholino VIsualisation of Expression (MOVIE)[32] (Fig. 5A). *miR430* genes are among the first and most transcribed genes in fish, and hence, an excellent candidate to assess zygotic transcription onset[33]. In most embryos, we observed the first instances of *miR430* transcription in division round 9. Interestingly, we found that the expression was initiated in a graded manner during division rounds 9 and 10, first appearing in cells close to the margin, followed by cells in the intermediate zone between the margin and AP, and last in cells at the AP (Figs. 5B, S5, Movie S10).

This suggests that zygotic transcription onset occurs as a spatiotemporal gradient along the AP-margin axis (Figs. 5B, S5). To determine whether this zygotic transcription onset pattern arises due to the gradient of cell volume and/or cell cycle length along this axis, we examined bi-lobed embryos, where both gradients are perturbed (Figs. 4A-B, 5C). Importantly, unlike in control embryos, cells at the AP in bi-lobed embryos are smaller and cycle slower than those in the intermediate zone (Figs. 4A-B). Analysis of these bi-lobed embryos showed that, in contrast to control embryos, *miR430* transcription was first initiated at the embryonic margin and the AP, where cells were smallest in these embryos before it did in the intermediate zone (Fig. 5D, Movie S11). This suggests that the gradient of cell volume and/or cell cycle length along the AP-margin axis influences the onset of zygotic transcription along this axis, thereby spatiotemporally linking early embryo geometry to the onset of zygotic gene expression.

Discussion

Our work connects embryo geometry to asymmetric cell divisions and cell volume distribution and shows that the volume distribution influences cell cycle length and zygotic gene transcription. Previously, we demonstrated that the blastodisc in the fertilized egg, from which all embryonic cells originate, attains its specific shape during ooplasmic streaming[30]. This shape is defined by the egg plasma membrane on one side and yolk granules on the other. Our data suggest that if the mitotic spindle consistently aligns with the longest cell axis, known as Hertwig's rule, this alone can explain how the initial shape of the blastodisc leads to unequal cell divisions during successive reductive cleavage divisions, ultimately creating a gradient of cell volumes along the animal-to-margin axis of the forming blastoderm. While this does not rule out the involvement of more complex mechanisms - such as differential interactions between spindle microtubules and yolk granules versus the cellular cortex or plasma membrane - it indicates that such complexities are not necessary to account for the observed outcomes.

Furthermore, our work provides evidence that the cell volume gradient influences the cell cycle length gradient by establishing a gradient in the nucleocytoplasmic (N/C) ratio, which has been previously implicated in controlling cell cycle length[10]. Various mechanisms have been proposed for how the N/C ratio regulates cell cycle length, primarily focusing on its impact on the availability and activity of cell cycle regulators[8,9,11,12]. While our findings support the role of the N/C ratio in determining cell cycle length and that of the cell cycle regulator Chek1 therein, they do not pinpoint a specific underlying mechanism. Notably, although our observations align with the idea that cell volume regulation is the primary mechanism for cell cycle synchronization in the embryo, additional factors may also modulate this process. For instance, synchronization during early cleavage stages might be facilitated by cytoplasmic bridges connecting cells at early cleavage stages, allowing mitotic trigger waves to propagate through these connections and synchronize cell cycles. Such transient coupling of cells at early, but not later, cleavage stages is consistent with our mathematical simulations, which suggest that the observed evolution of mitotic timing variance in wild-type embryos is best described by an exponential decay in coupling strength across successive division rounds.

Finally, there are multiple potential mechanisms linking the cell volume and/or cell cycle gradients to the onset of zygotic gene transcription. These mechanisms typically propose that either cell volume, and thus the N/C ratio, promotes transcription by the DNA titrating transcriptional repressors, or that a short cell cycle length inhibits transcription by causing competition between the

DNA replication and transcription machineries. Our observation that the smaller, slower-cycling cells at the blastoderm margin not only initiate zygotic transcription before the larger, faster-cycling cells at the animal pole but also continue transcription for a longer duration supports the idea that cell cycle length determines the spatiotemporal pattern of zygotic gene transcription. This finding is significant, as it suggests that the regulation of cell cycle synchronization by the cell volume gradient is crucial for its influence on the patterning of zygotic genome activation.

Robust regulation of Zygotic Genome Activation (ZGA) is essential for accurate cell fate specification and associated morphogenetic processes. Given its importance, one would assume that the factors regulating ZGA must also be robust themselves. Considering that embryo shape is one of the most distinct and invariant features of animal development, it is plausible that it serves as a major determinant of ZGA and its regulated processes. Several observations support this notion. For instance, in zebrafish embryos, smaller and slower-cycling cells near the margin initiate zygotic transcription first and subsequently adopt the mesendodermal fate, suggesting that early zygotic gene activation may facilitate this process. Similar observations were also made in sea urchins and nematodes, with smaller cells at the vegetal pole (micromeres) of sea urchin embryos cycling slower than larger cells and later assuming a mesodermal fate, and lineages producing cells in *C. elegans* embryos that involute during gastrulation also exhibiting slower cell cycles compared to non-involuting cells. Collectively, these previous findings underscore the physiological significance of our observation that the spatiotemporal patterning of ZGA is the product of embryo shape determining the distribution of cell volumes and cell cycle lengths within the early embryo. The specific developmental consequences of this fundamental relationship will likely differ between different species and need to be explored in the specific organismal context.

Methods

Cell cycle analysis

Tg(*actb2:rfp-pcna*) embryos were dechorionated and, at the desired stage, mounted in 0.5% agarose gels prepared in E3 buffer with the animal pole facing upward in casts made with 2% agarose solution in E3 buffer[14]. RFP fluorescence was imaged at 23.5 °C using a 20x water-dipping objective on Zeiss LSM800 (N.A.=0.8), LSM880 (N.A.=1.0), or LSM900 (N.A.=1.0) upright confocal microscopes. 200-350 µm-thick Z-stacks were acquired for different experiments with temporal resolutions ranging between 17-65 sec/Z-stack. The presence or absence of nuclear RFP-PCNA fluorescence was used to determine if a cell was in the S or M phase of the cell cycle, respectively[34–36]. The nuclear signal was segmented in Fiji using the Labkit plugin[37,38]. The segmented objects were imported into Bitplane Imaris (https://imaris.oxinst.com/) to generate tracks and obtain tracking-related data, including track start time (S-phase entry), track end time (M-phase entry), track duration (S-phase length), and the nuclear coordinates at the last S-phase time point (position). These data were then analyzed using the Pandas Python library to calculate, for instance, the division timing variance in a given division round, followed by plotting using mainly the Matplotlib and Seaborn libraries[39–41]. Anaphase onset timings for comparison between sister and non-sister cells were determined by generating 3D image stacks of wild-type AB embryos injected with 0.5 pg Histone 1-Alexa Fluor 488 (Catalog #H13188, Invitrogen) at the one-cell stage as described above.

Mitotic wave speed

The mitotic wave speed for a given round of division was determined by first identifying the position of the wave origin and the timing of the wave origination, measuring all other nuclear distances and

mitotic entry timings relative to this position and time, and then generating the best fitting distance-time linear curve. In the cases where more than one nucleus could be considered the origin of the mitotic wave due to a simultaneous entry into mitosis, the mean of the 3D coordinates of such nuclei was considered the position of the wave origin.

Microinjections

To visualize cell cycle progression using Histone 1 as the marker, 0.5 pg Histone 1-Alexa Fluor 488 was injected at the one-cell stage into wild-type AB or Tg(*actb2:lyn-tdTomato*) embryos[42]. Mosaic perturbation of the cycling period of a subset of the cells was carried out by mounting 32/64-cell stage embryos in 2% agarose solution in E3 buffer and injecting 0.2-0.3 pg of Histone 1-Alexa Fluor 488 into such cells. *chek1* overexpression was achieved by injecting 12 pg *chek1* mRNA into the one-cell embryo[13,41]. mRNA was prepared as described previously[20].

Drug treatments

Aurkb function was inhibited by transiently incubating dechorionated <5 min post fertilization (mpf) embryos in 50 µM AZD1152 (Catalog #SML0268, Sigma-Aldrich) solution for 15 min, after which they were returned to E3 buffer. Embryos showing successful nuclear cycling despite a failure of cytokinesis were then imaged as described above. Inhibition of Aurkb function concomitantly with *chek1* overexpression or Histone 1-Alexa Fluor 488 visualization was performed by injecting 12 pg *chek1* mRNA or 0.5 pg Histone 1-Alexa Fluor 488, respectively, at the one-cell stage as described above, followed by incubation in the Aurkb inhibitor. Chek1 activity inhibition was performed by dechorionating <10 mpf embryos and incubating them in 10 µM PF477736 (Catalog #HY-10032, MedChem Express) solution in E3 buffer throughout the duration of analysis.

Nuclear volume measurement

Nuclear RFP-PCNA fluorescence was segmented from Z-stacks by thresholding using Fiji, and their volumes were measured using the 3D Objects Counter plugin[43].

Cell volume measurement

Cell volumes at the 8- and 16-cell stages were measured by semi-automatically generating cell segmentation using the ‘Contour’ function for surface creation in Bitplane Imaris from Z-stacks of Tg(*actb2:mCherry-CAAX*) embryos[44]. Once segmented, the physical attributes of individual cells, such as volume and position, were exported from Bitplane Imaris as CSV files. The last time point before the onset of the fourth or fifth mitotic round was used to measure the cell volume for the 8- or the 16-cell stage, respectively. Cell volumes at the 128-cell stage were measured by generating cell segmentations using the Limeseg plugin in Fiji and exporting the cell volume data for individual segmented objects[45]. All downstream data analysis was performed in Python, mainly using the Pandas library, and the plots were produced using the Matplotlib and Seaborn libraries.

Daughter cell volume prediction

Cell surfaces generated in Bitplane Imaris at the 8-cell stage were exported as WRL files, imported into MeshLab (https://www.meshlab.net/), from where individual cell surfaces were exported as PLY files. These files were subsequently processed in Python to identify the longest cell axis by performing Principal Component Analysis (PCA), along which the cell was bisected into two daughter cells representing cells at the 16-cell stage[29].

Nearest neighbor distance calculation

Nuclei positions were obtained from Bitplane Imaris, as detailed above. For each nucleus, the three nearest neighbors were identified, and their mean distance from the reference nucleus was calculated using the Pandas library in Python.

Cytoplasm aspiration

Approximately 30 mpf Tg(*actb2:rfp-pcna*) embryos were mounted in E3 buffer on a substrate prepared with 2% agarose solution in E3 buffer. A 20 µm blunt-end needle attached to a 10 µl Hamilton syringe was inserted through the yolk into the blastodisc, and the cytoplasm was carefully aspirated. The nuclear RFP-PCNA signal was constantly observed using a Leica stereo-fluorescence microscope to ensure the nucleus was not extracted together with the cytoplasm.

Nucleus aspiration

The setup and mounting procedure for the nucleus aspiration were the same as for cytoplasm aspiration described above, except that, in this case, the nucleus was aspirated rather than the cytoplasm and from embryos at the two-cell stage rather than the one-cell stage. Care was exercised to ensure that the nucleus was extracted with a negligible volume of the cytoplasm being aspirated in the process.

Generation of bi-lobed embryos

Bi-lobed embryos were created by spatially confining dechorionated embryos at the two-cell stage, still undergoing cytokinesis from the first division round, in 0.5-0.6% agarose in E3 buffer. Microscopy was performed as described above.

Yolk severing

To sever the yolk, dechorionated embryos at the two-cell stage were placed on a substrate of 3% methylcellulose in E3 buffer in a glass dish. Using an eyelash attached to the end of a Pasteur pipette, the vegetal half of the yolk was first punctured to prevent the embryo from exploding due to a buildup of internal pressure during the severing procedure and then carefully sliced. The embryo was allowed to recover for at least 15 minutes after the procedure, followed by mounting and microscopy, as detailed above.

Cell division angle measurement

Four orthogonal sections, each showing four nuclei along the 4th round division plane at the 16-cell stage, were generated using the Fiji Reslice function from Z-stacks of individual Tg(*actb2:rfp-pcna*) embryos. The angles between nuclei were then measured using Fiji, as represented in Fig. 4D, to obtain the angle of cell divisions in the 4th division round.

miR430 transcription analysis

pri-*miR430* transcripts were labelled as described previously[14]. Tg(*actb2:rfp-pcna*) embryos injected with MO1-3-Fluorescein (Gene Tools) at the one-cell stage were mounted in 0.5% agarose solution in E3 buffer in #3 Fluorinated ethylene propylene (FEP) tubes, and Z-stacks were generated with a temporal resolution of approximately one min/Z-stack using a 20x/N.A. 1.33 objective on a Zeiss

Lightsheet 7 microscope. Maximum intensity projections of these time-lapse recordings were then used to assess the transcription status of individual nuclei.

References

1. Deneke, V. E., Melbinger, A., Vergassola, M. & Di Talia, S. Waves of Cdk1 Activity in S Phase Synchronize the Cell Cycle in Drosophila Embryos. *Dev. Cell* **38**, 399–412 (2016).
2. Chang, J. B. & Ferrell, J. E. Mitotic trigger waves and the spatial coordination of the Xenopus cell cycle. *Nature* **500**, 603–607 (2013).
3. Anderson, G. A., Gelens, L., Baker, J. C. & Ferrell, J. E. Desynchronizing Embryonic Cell Division Waves Reveals the Robustness of Xenopus laevis Development. *Cell Rep.* **21**, 37–46 (2017).
4. Kimmel, C. B., Ballard, W. W., Kimmel, S. R., Ullmann, B. & Schilling, T. F. Stages of embryonic development of the zebrafish. *Dev. Dyn.* **203**, 253–310 (1995).
5. Kane, D. A. & Kimmel, C. B. The zebrafish midblastula transition. *Dev. Camb. Engl.* **119**, 447–456 (1993).
6. Petridou, N. I., Grigolon, S., Salbreux, G., Hannezo, E. & Heisenberg, C.-P. Fluidization-mediated tissue spreading by mitotic cell rounding and non-canonical Wnt signalling. *Nat. Cell Biol.* **21**, 169–178 (2019).
7. Shen, W. *et al.* Comprehensive maturity of nuclear pore complexes regulates zygotic genome activation. *Cell* **185**, 4954-4970.e20 (2022).
8. Newport, J. & Kirschner, M. A major developmental transition in early Xenopus embryos: I. characterization and timing of cellular changes at the midblastula stage. *Cell* **30**, 675–686 (1982).
9. Newport, J. & Kirschner, M. A major developmental transition in early xenopus embryos: II. control of the onset of transcription. *Cell* **30**, 687–696 (1982).
10. Langley, A. R., Smith, J. C., Stemple, D. L. & Harvey, S. A. New insights into the maternal to zygotic transition. *Development* **141**, 3834–3841 (2014).
11. Edgar, B. A. & Schubiger, G. Parameters controlling transcriptional activation during early drosophila development. *Cell* **44**, 871–877 (1986).
12. Kimelman, D., Kirschner, M. & Scherson, T. The events of the midblastula transition in Xenopus are regulated by changes in the cell cycle. *Cell* **48**, 399–407 (1987).

13. Zamir, E., Kam, Z. & Yarden, A. Transcription-Dependent Induction of G1 Phase during the Zebra Fish Midblastula Transition. *Mol. Cell. Biol.* **17**, 529–536 (1997).

14. Boothe, T. *et al.* A tunable refractive index matching medium for live imaging cells, tissues and model organisms. *eLife* **6**, e27240 (2017).

15. Keller, P. J., Schmidt, A. D., Wittbrodt, J. & Stelzer, E. H. K. Reconstruction of zebrafish early embryonic development by scanned light sheet microscopy. *Science* **322**, 1065–1069 (2008).

16. Olivier, N. *et al.* Cell Lineage Reconstruction of Early Zebrafish Embryos Using Label-Free Nonlinear Microscopy. *Science* **329**, 967–971 (2010).

17. Berloco, M., Fanti, L., Breiling, A., Orlando, V. & Pimpinelli, S. The maternal effect gene, abnormal oocyte (abo), of Drosophila melanogaster encodes a specific negative regulator of histones. *Proc. Natl. Acad. Sci.* **98**, 12126–12131 (2001).

18. Gunjan, A. & Verreault, A. A Rad53 Kinase-Dependent Surveillance Mechanism that Regulates Histone Protein Levels in S. cerevisiae. *Cell* **115**, 537–549 (2003).

19. Brown, D. T., Alexander, B. T. & Sittman, D. B. Differential effect of H1 variant overexpression on cell cycle progression and gene expression. *Nucleic Acids Res.* **24**, 486–493 (1996).

20. Petridou, N. I., Corominas-Murtra, B., Heisenberg, C.-P. & Hannezo, E. Rigidity percolation uncovers a structural basis for embryonic tissue phase transitions. *Cell* **184**, 1914-1928.e19 (2021).

21. Kuramoto, Y. *Chemical Oscillations, Waves, and Turbulence*. vol. 19 (Springer, Berlin, Heidelberg, 1984).

22. Nolet, F. E. *et al.* Nuclei determine the spatial origin of mitotic waves. *eLife* **9**, e52868 (2020).

23. Murata-Hori, M., Tatsuka, M. & Wang, Y.-L. Probing the Dynamics and Functions of Aurora B Kinase in Living Cells during Mitosis and Cytokinesis. *Mol. Biol. Cell* **13**, 1099–1108 (2002).

24. Kimmel, C. B. & Law, R. D. Cell lineage of zebrafish blastomeres: I. Cleavage pattern and cytoplasmic bridges between cells. *Dev. Biol.* **108**, 78–85 (1985).

25. Conn, C. W., Lewellyn, A. L. & Maller, J. L. The DNA Damage Checkpoint in Embryonic Cell Cycles Is Dependent on the DNA-to-Cytoplasmic Ratio. *Dev. Cell* **7**, 275–281 (2004).

26. Piñeros, L. *et al.* The nuclear-cytoplasmic ratio controls the cell cycle period in compartmentalized frog egg extract. 2024.07.28.605512 Preprint at https://doi.org/10.1101/2024.07.28.605512 (2024).

27. Minc, N., Burgess, D. & Chang, F. Influence of Cell Geometry on Division-Plane Positioning. *Cell* **144**, 414–426 (2011).

28. Hertwig, O. *Das Problem der Befruchtung und der Isotropie des Eies: eine Theorie der Vererbung*. (Verlag von Gustav Fischer, 1884).

29. Wold, S., Esbensen, K. & Geladi, P. Principal component analysis. *Chemom. Intell. Lab. Syst.* **2**, 37–52 (1987).

30. Shamipour, S. *et al.* Bulk Actin Dynamics Drive Phase Segregation in Zebrafish Oocytes. *Cell* **177**, 1463-1479.e18 (2019).

31. Danilova, N. *et al.* The role of the DNA damage response in zebrafish and cellular models of Diamond Blackfan anemia. *Dis. Model. Mech.* **7**, 895–905 (2014).

32. Hadzhiev, Y. *et al.* A cell cycle-coordinated Polymerase II transcription compartment encompasses gene expression before global genome activation. *Nat. Commun.* **10**, 691 (2019).

33. Heyn, P. *et al.* The Earliest Transcribed Zygotic Genes Are Short, Newly Evolved, and Different across Species. *Cell Rep.* **6**, 285–292 (2014).

34. Budke, H. *et al.* Assessment of cell proliferation in paraffin sections of normal bone marrow by the monoclonal antibodies Ki-67 and PCNA. *Mod. Pathol.* **7**, 860–866 (1994).

35. Kelman, Z. PCNA: structure, functions and interactions. *Oncogene* **14**, 629–640 (1997).

36. Leung, A. Y. *et al.* Proliferating cell nuclear antigen (PCNA) as a proliferative marker during embryonic and adult zebrafish hematopoiesis. *Histochem. Cell Biol.* **124**, 105–111 (2005).

37. Schindelin, J. *et al.* Fiji: an open-source platform for biological-image analysis. *Nat. Methods* **9**, 676–682 (2012).

38. Arzt, M. *et al.* LABKIT: Labeling and Segmentation Toolkit for Big Image Data. *Front. Comput. Sci.* **4**, (2022).

39. McKinney, W. Data Structures for Statistical Computing in Python. in 56–61 (Austin, Texas, 2010). doi:10.25080/Majora-92bf1922-00a.

40. Hunter, J. D. Matplotlib: A 2D Graphics Environment. *Comput. Sci. Eng.* **9**, 90–95 (2007).

41. Waskom, M. L. seaborn: statistical data visualization. *J. Open Source Softw.* **6**, 3021 (2021).

42. Stegmaier, J. *et al.* Real-Time Three-Dimensional Cell Segmentation in Large-Scale Microscopy Data of Developing Embryos. *Dev. Cell* **36**, 225–240 (2016).

43. Bolte, S. & Cordelières, F. P. A guided tour into subcellular colocalization analysis in light microscopy. *J. Microsc.* **224**, 213–232 (2006).

44. Tavano, S. *et al.* BMP-dependent patterning of ectoderm tissue material properties modulates lateral mesendoderm cell migration during early zebrafish gastrulation. 2023.07.21.550024 Preprint at https://doi.org/10.1101/2023.07.21.550024 (2023).

45. Machado, S., Mercier, V. & Chiaruttini, N. LimeSeg: a coarse-grained lipid membrane simulation for 3D image segmentation. *BMC Bioinformatics* **20**, 2 (2019).

Fig. 1

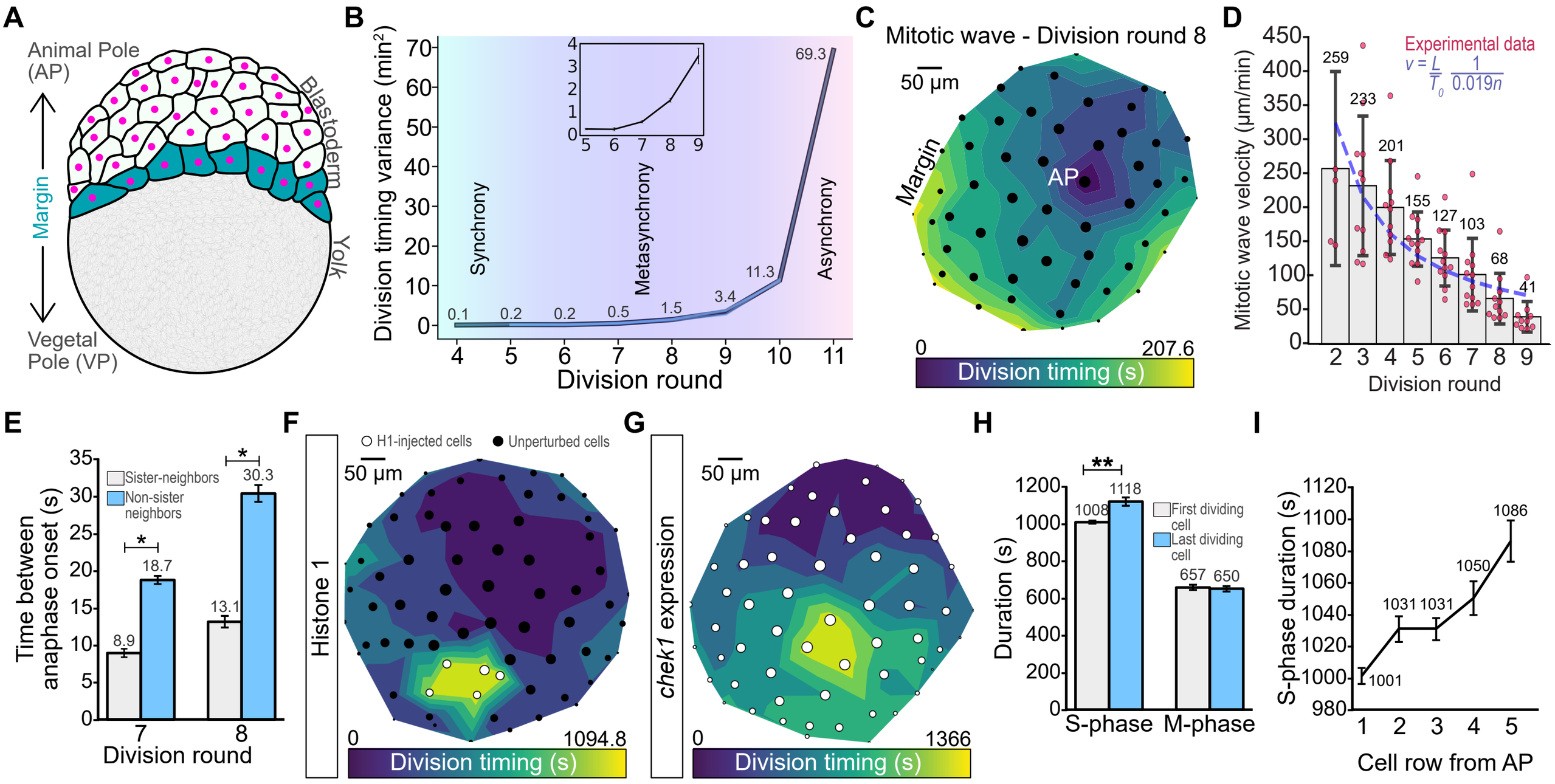
A
Animal Pole (AP)
Margin
Vegetal Pole (VP)
Blastoderm
Yolk
B
Division timing variance (min²)
Division round
Synchrony
Metasynchrony
Asynchrony
0.1
0.2
0.2
0.5
1.5
3.4
11.3
69.3
C
Mitotic wave - Division round 8
50 µm
Margin
AP
0
207.6
Division timing (s)
D
Mitotic wave velocity (µm/min)
Division round
Experimental data
$v = \frac{L}{T_0} \frac{1}{0.019n}$
259
233
201
155
127
103
68
41
E
Time between anaphase onset (s)
Division round
Sister-neighbors
Non-sister neighbors
8.9
18.7
13.1
30.3
F
Histone 1
H1-injected cells
Unperturbed cells
50 µm
0
1094.8
Division timing (s)
G
chek1 expression
50 µm
0
1366
Division timing (s)
H
Duration (s)
First dividing cell
Last dividing cell
1008
1118
657
650
S-phase
M-phase
I
S-phase duration (s)
Cell row from AP
1001
1031
1031
1050
1086

Fig. 1: Mitotic synchrony gradually decreases as the S-phase lengthens along the animal-margin axis.

(A) Schematic representation of a zebrafish embryo at late cleavage stage. The blastoderm is positioned at the animal pole (AP) atop the yolk cell at the vegetal pole (VP). The last row of blastoderm cells (cyan) constitutes the margin. (B) Line plot of cell division timing variance in Tg(*actb2:rfp-pcna*) embryos for cleavage division rounds 4-11. Blue lines, individual embryos; black line, mean across 4 embryos. Inset shows variance for division rounds 5-9 (C) Contour plot of the radial mitotic wave across all surface cells at the 8th cleavage division round in a representative wild-type embryo. Each dot represents the position of a nucleus along the XY plane, and the size of the dot indicates its position along the Z-axis (AP-margin axis). Colors represent division timing for each nucleus. (D) Bar plot of mitotic wave velocities (mean ± SD), calculated by generating distance-time plots, for cleavage division rounds 2-9, with the red dots showing wave velocities for individual embryos. n=5-11 embryos. Blue dotted line: Curve described by the equation $v=(L/T_0).(1/0.019n)$, where L is the total AP-margin distance, T_0 is the cell cycle period at the AP, and n is the division round to represent the effect of a 1.9% period gradient along the AP-margin axis on mitotic wave speeds. (E) Bar plot of delay in anaphase onset between sister and non-sister neighbor cells (mean ± SEM) as a readout for cell division synchrony. n≥19 cell pairs; Student's t-test with $p<0.05$]. (F,G) Representative contour plots of mitotic waves at the 8th round of division in embryos injected with either 0.3pg Histone 1A protein into a single blastomere at the 32-cell stage (F) or 12pg *chek1* mRNA at the 1-cell stage. (H) Bar plot of M-phase and S-phase lengths (mean ± SD) at the 8th cleavage division round. n=8 embryos; Student's t-test with $p<0.01$]. (I) Line plot of S-phase duration (mean ± SEM) as a function of cell position relative to the AP. n≥4 embryos.

Fig. 2

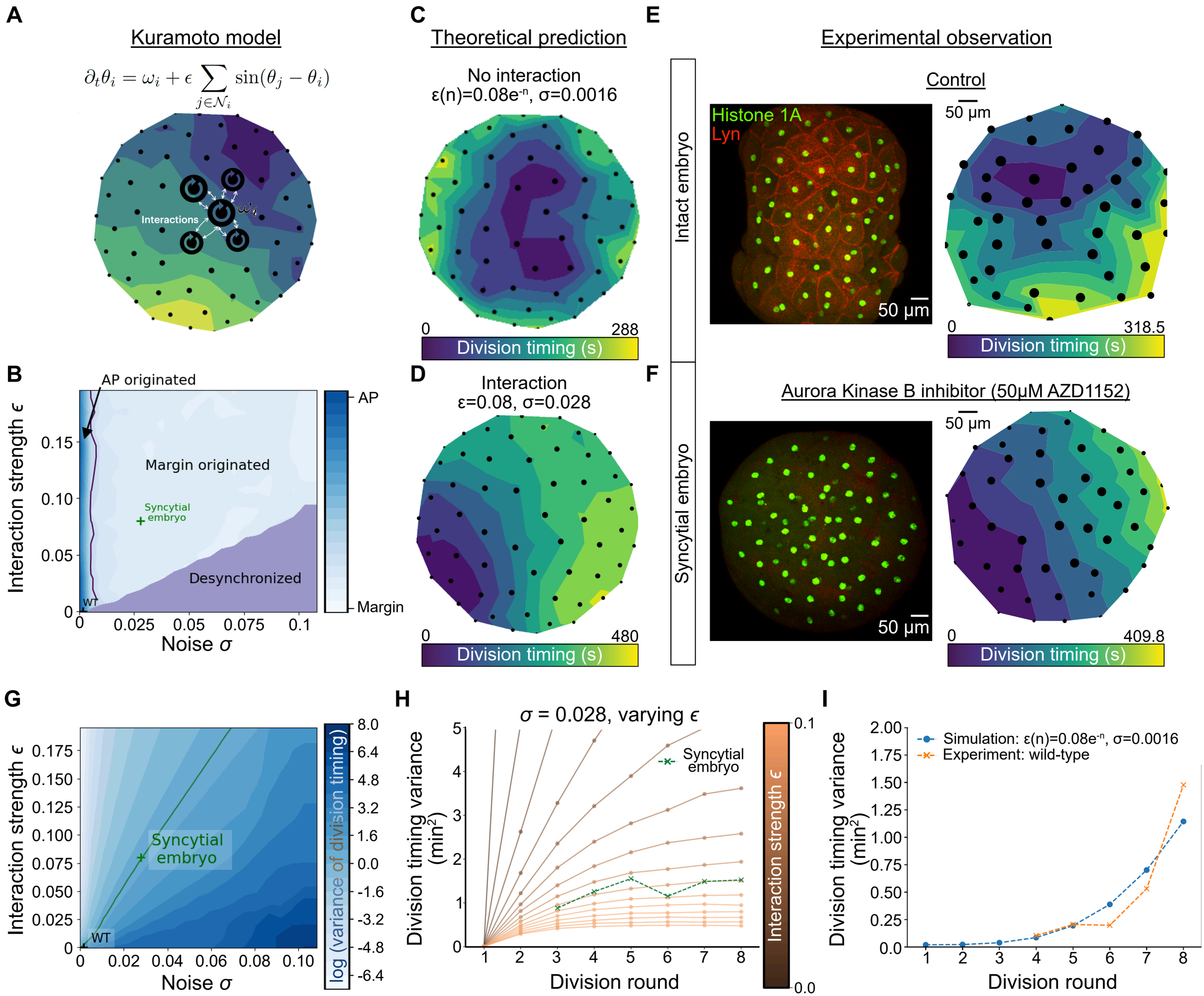
A
Kuramoto model
$\partial_t \theta_i = \omega_i + \epsilon \sum_{j \in \mathcal{N}_i} \sin(\theta_j - \theta_i)$
Interactions
ω_i
B
AP originated
Margin originated
Syncytial embryo
Desynchronized
WT
Interaction strength ϵ
Noise σ
AP
Margin
C
Theoretical prediction
No interaction
ε(n)=0.08e^-n, σ=0.0016
0
288
Division timing (s)
D
Interaction
ε=0.08, σ=0.028
0
480
Division timing (s)
E
Experimental observation
Control
Intact embryo
Histone 1A
Lyn
50 μm
0
318.5
Division timing (s)
F
Aurora Kinase B inhibitor (50μM AZD1152)
Syncytial embryo
50 μm
0
409.8
Division timing (s)
G
Syncytial embryo
WT
Interaction strength ϵ
Noise σ
log (variance of division timing)
H
σ = 0.028, varying ϵ
Syncytial embryo
Division timing variance (min²)
Division round
Interaction strength ϵ
I
Simulation: ε(n)=0.08e^-n, σ=0.0016
Experiment: wild-type
Division timing variance (min²)
Division round

Fig. 2: Cell-cell coupling repositions the mitotic wave origin to the margin and prevents desynchronization.

(A) Schematic representation of our adapted Kuramoto model and the equation describing the evolution of the phase of a cell cycle. Equation: θ_i represents the cell cycle phase of cell *i*, and N_i denotes its nearest neighboring cells, determined through Delaunay triangulation of the hemisphere. The coupling strength ϵ represents how strongly each cell influences its neighbors' timing. The intrinsic frequency ω_i represents how quickly cell *i* would progress through its cell cycle in isolation. Model: Each black dot represents a cell positioned on a hemispherical Fibonacci lattice. Dot size increases with height (*z*) to aid visualization in this top-down projection. Lines between dots (not shown) indicate coupled neighbors that can influence each other's cell cycle timing. (B) Phase diagram showing origin of the waves in ε-σ space. The boundary between AP originated and margin originated is thresholded at z=0.5 and the region of desynchronization corresponds to $\langle e^{i\theta_j}\rangle_j < 0.6$, where $\langle\rangle_j$ denotes averaging over all sites. (C) Contour plot of the radial mitotic wave across all surface cells at the 8th cleavage division round as predicted using the Kuramoto model of interacting oscillators, assuming an AP-margin period gradient of 1.9% and exponentially decaying cell-cell interaction strength ($\varepsilon=0.08e^{-n}$, σ=0.0016). (D) Contour plot of the mitotic wave across all surface cells at the 8th cleavage division round as predicted using the Kuramoto model of interacting oscillators, assuming an AP-margin period gradient of 1.9% and partial interaction between cells (ε=0.08, σ=0.028). (E) Left: Representative image of a 128-cell stage control Tg(*actb2:lyn-tdtomato*) embryo injected with 1pg Histone1A-Alexa Fluor 488 at the one-cell stage to show the presence of plasma membrane between individual nuclei. Right: Contour plot of the radial mitotic wave across all surface cells at the 8th cleavage division round observed in a control embryo, where nuclear divisions were visualized using either Histone1A-Alexa Fluor 488 injections or using Tg(*actb2:rfp-pcna*) embryos. n=7 embryos. (F) Left: Representative image of a 128-cell stage Tg(*actb2:lyn-tdtomato*) embryo injected with 1pg Histone1A-Alexa Fluor 488 at the one-cell stage and treated with 50µM AZD1152 to show the absence of plasma membrane between individual nuclei. Right: Contour plot of the mitotic wave across all surface cells at the 8th cleavage division round observed in a representative syncytial embryo, where nuclear divisions were visualized using either Histone1A-Alexa Fluor 488 injections or using Tg(*actb2:rfp-pcna*) embryos. n=7 embryos. (G) Phase diagram of the Kuramoto model in ε-σ space. The log of the variance of the

division timings at the 8th round is plotted. The green solid line indicates the contour line of the observed variance at the 8th round in syncytial embryos. (H) Variances of division timings for each round for fixed noise value, σ=0.028 as ε varies. Green dotted curve shows the variances measured in syncytial embryos. (I) Variances of division timings for each round in wild-type embryos (orange) fitted with a curve described by exponentially decaying interaction strength, $\varepsilon(n)=0.08e^{-n}$, and low noise, σ=0.0016 (blue).

Fig. 3

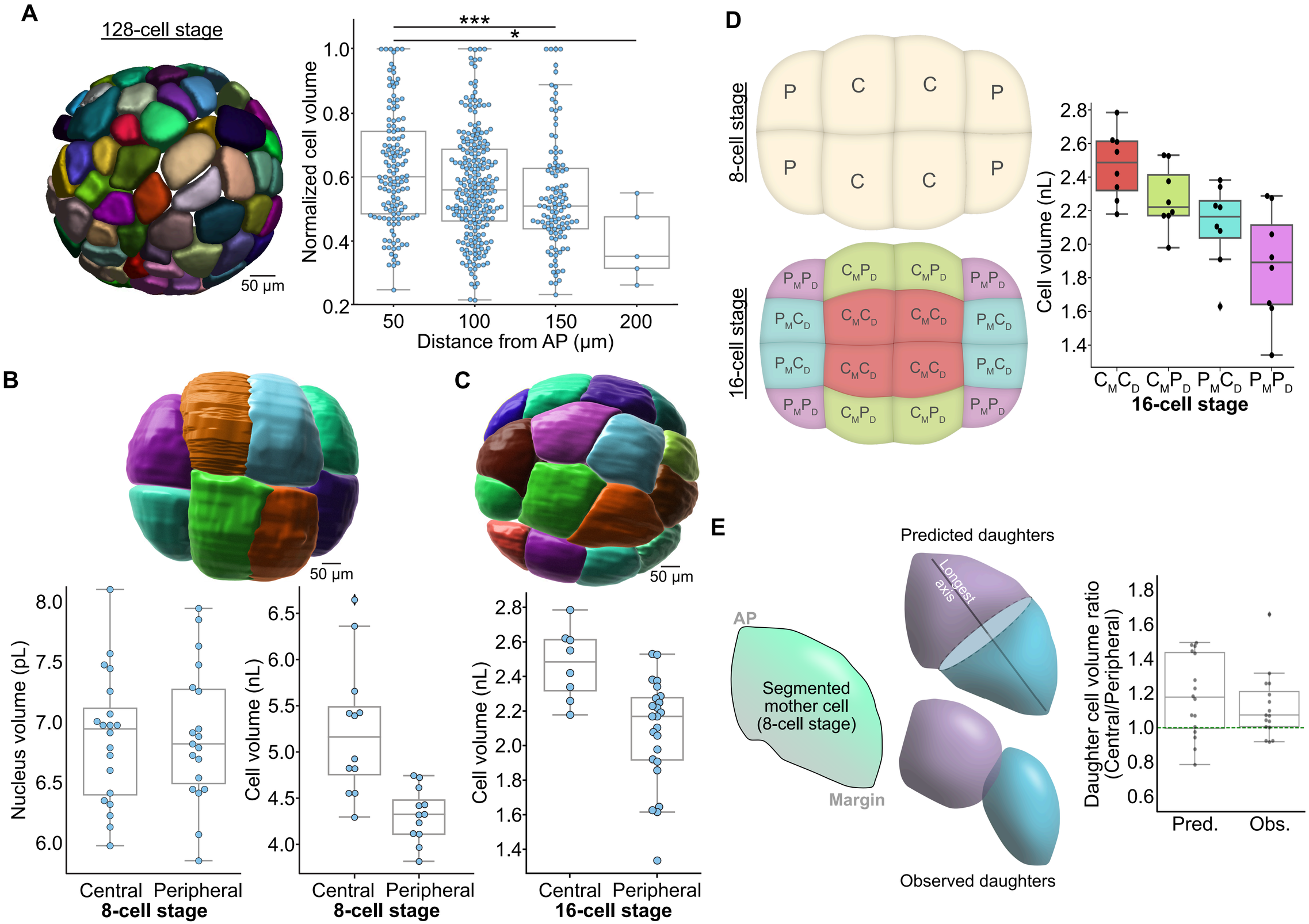
A
128-cell stage
50 µm
***
*
Normalized cell volume
1.0
0.8
0.6
0.4
0.2
50
100
150
200
Distance from AP (µm)
B
50 µm
C
50 µm
Nucleus volume (pL)
8.0
7.5
7.0
6.5
6.0
Central
Peripheral
8-cell stage
Cell volume (nL)
6.5
6.0
5.5
5.0
4.5
4.0
Central
Peripheral
8-cell stage
Cell volume (nL)
2.8
2.6
2.4
2.2
2.0
1.8
1.6
1.4
Central
Peripheral
16-cell stage
D
8-cell stage
P
C
C
P
P
C
C
P
16-cell stage
P_MP_D
C_MP_D
C_MP_D
P_MP_D
P_MC_D
C_MC_D
C_MC_D
P_MC_D
P_MC_D
C_MC_D
C_MC_D
P_MC_D
P_MP_D
C_MP_D
C_MP_D
P_MP_D
Cell volume (nL)
2.8
2.6
2.4
2.2
2.0
1.8
1.6
1.4
C_MC_D
C_MP_D
P_MC_D
P_MP_D
16-cell stage
E
AP
Segmented mother cell (8-cell stage)
Margin
Predicted daughters
Longest axis
Observed daughters
Daughter cell volume ratio (Central/Peripheral)
1.8
1.6
1.4
1.2
1.0
0.8
0.6
Pred.
Obs.

Fig. 3: Embryo geometry drives asymmetric cell divisions to generate a gradient of cell volumes in the early embryo.

(A) Representative image of a 128-cell stage embryo (round 8) with surface cells segmented (left) and box-plot showing normalized cell volumes as a function of cell position with respect to the AP (right). Cell volumes were internally normalized by dividing each cell volume by the volume of the largest cell in the embryo. Each dot represents the data for an individual cell. (n=469 cells, 12 embryos). (B) Representative image of an 8-cell stage embryo (round 4) with surface cells segmented (top) and box-plot showing volumes of individual nuclei and cells based on their position relative to the AP (bottom). 'Central' cells are positioned at AP, whereas 'peripheral' cells are positioned away from the AP (n=20 central and 19 peripheral nuclei, 5 embryos; 12 central and 12 peripheral cells, 3 embryos). (C) Representative image of a 16-cell stage embryo (round 5) with surface cells segmented (top) and box-plot showing volumes of individual cells based on their position relative to the AP (bottom; n=8 central and 24 peripheral cells, 2 embryos). (D) Schematic showing the lineage relationship between cells at the 8-cell stage (top-left) and the 16-cell stage (bottom-left). At the 8-cell stage, cells marked 'C' are centrally positioned, and those marked 'P' are peripherally positioned. At the 16-cell stage, cells are labelled to indicate both their positions (C_D, centrally; P_D, peripherally) and the identities of their mother cells (C_M, centrally positioned mother cell; P_M, peripherally positioned mother cell). Box plot showing the distribution of cell volumes at the 16-cell stage based on each cell's position and lineage identity (right) (n=8 cells for each category, 2 embryos). (E) Schematic showing the pipeline for predicting daughter cell volumes at the 16-cell stage (left). Each segmented cell surface from the 8-cell stage was used to identify the longest cell axis, which was then bisected to obtain daughter cells at the 16-cell stage. Violin plot showing a comparison between the ratios of volumes of the central and peripheral daughter cells obtained from each cell division, respectively, either predicted (Pred.) or experimentally measured (Obs.) (right; n=16 cell pairs, 2 embryos).

Fig. 4

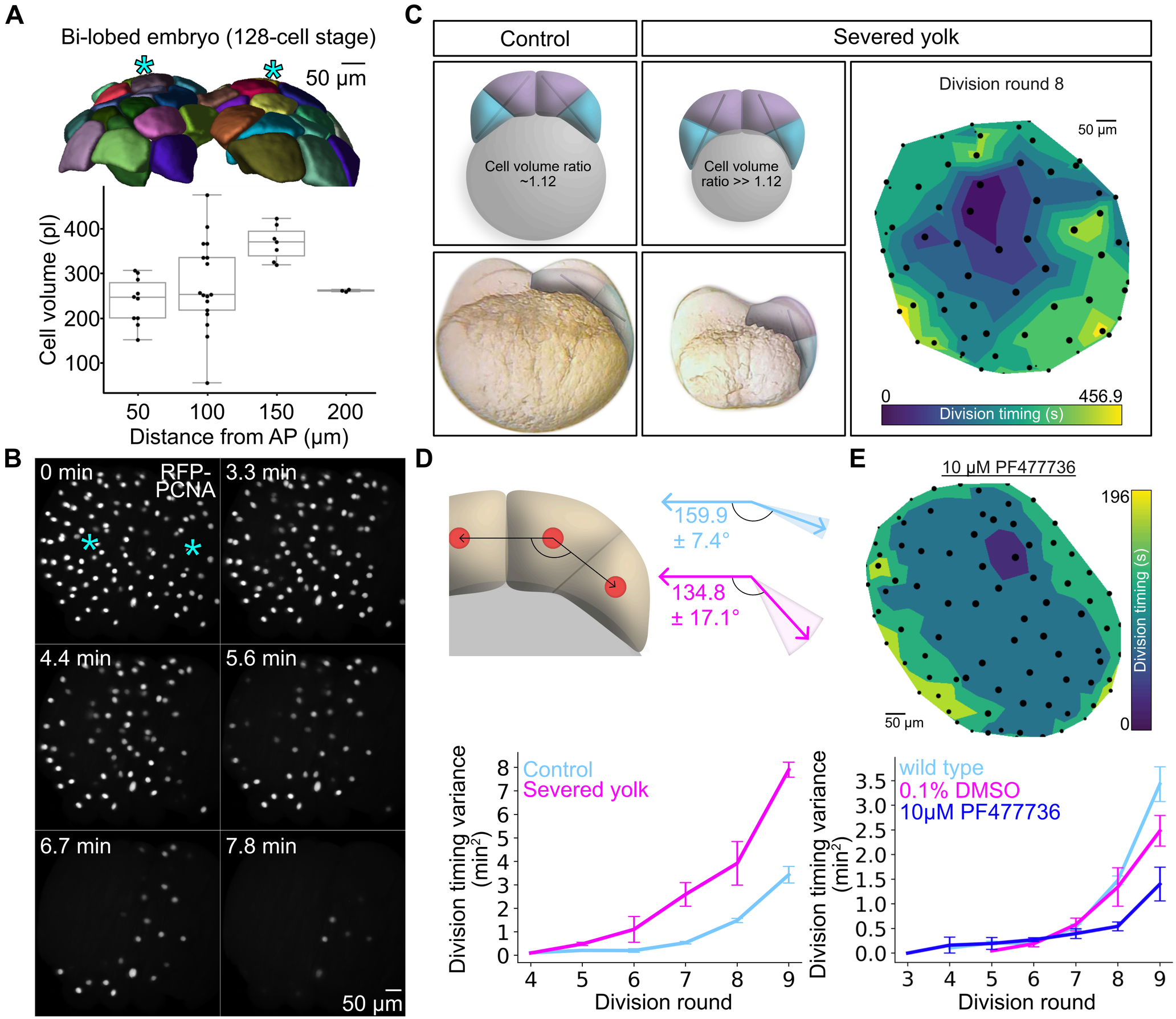
A
Bi-lobed embryo (128-cell stage)
50 µm
Cell volume (pl)
400
300
200
100
50
100
150
200
Distance from AP (µm)
B
0 min
RFP-PCNA
3.3 min
4.4 min
5.6 min
6.7 min
7.8 min
50 µm
C
Control
Severed yolk
Cell volume ratio ~1.12
Cell volume ratio >> 1.12
Division round 8
50 µm
0
456.9
Division timing (s)
D
159.9 ± 7.4°
134.8 ± 17.1°
Division timing variance (min²)
Control
Severed yolk
Division round
E
10 µM PF477736
196
0
Division timing (s)
50 µm
Division timing variance (min²)
wild type
0.1% DMSO
10µM PF477736
Division round

Fig. 4: AP-margin cell volume gradient increases cell cycle metasynchrony in a Chek1-dependent manner

(A) Representative image of a 128-cell stage (round 8) bi-lobed embryo with surface cells segmented (top) and box-plot showing normalized cell volumes as a function of cell position with respect to the AP (right) for this embryo. Cyan asterisks mark the ectopic animal poles in the bi-lobed embryo. (B) Montage of images showing the propagation of mitotic waves in a representative bi-lobed Tg(*actb2:rfp-pcna*) embryo at the 8th division round. Cyan asterisks mark the ectopic animal poles in the bi-lobed embryo (n=5 embryos). (C) Schematic representations (top-left) and representative images (bottom-left) of a control embryo and an embryo where the yolk has been severed at the two-cell stage to increase the curvature of the blastoderm-to-yolk cell interface. Lines inside the cells indicate the longest cell axis along which the divisions (division round 3) are expected to occur. Cells marked in magenta and cyan represent the resulting central and marginal daughter cells, respectively. Contour plot (right) shows mitotic wave propagation in the 8th division round of a yolk-severed embryo (AP-view). (D) Schematic representation (top) of the decreased angle of cell divisions in the 4th division round in yolk-severed embryos due to an increased curvature of the blastoderm-to-yolk cell interface compared to corresponding control embryos (angles are mean ± SD; n>10 cells). Line plot (bottom) showing the variance in cell division timings in control and yolk-severed embryos (mean ± SD; n=4 embryos). (E) Representative contour plot (top) showing mitotic wave propagation in a Chek1 inhibitor (PF477736)-treated embryo in division round 8 (AP-view). Line plot (bottom) showing the variance in cell division timings in control and PF477736-treated embryos (mean ± SD; n=4 embryos).

Fig. 5

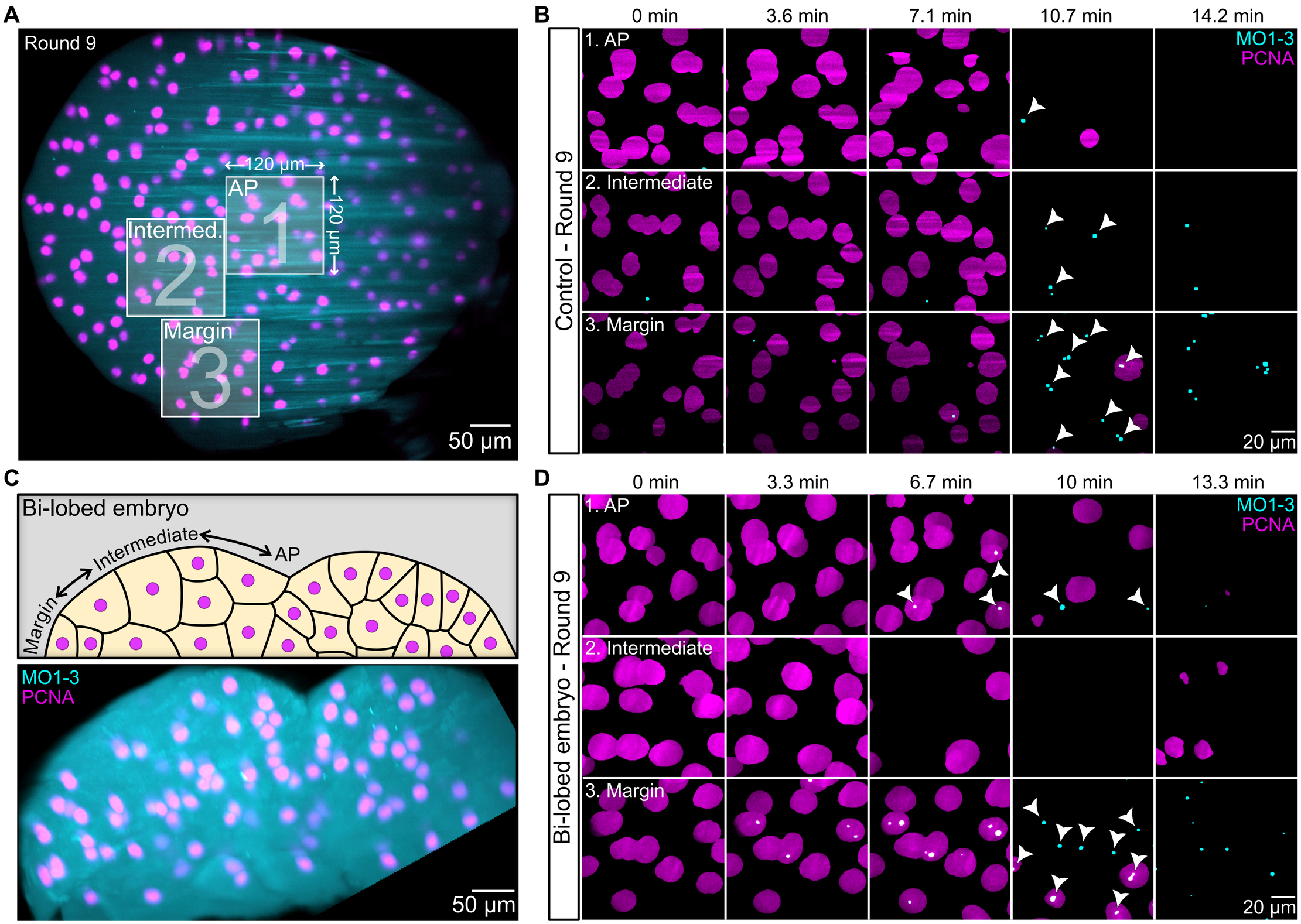
A
Round 9
120 µm
120 µm
AP
1
Intermed.
2
Margin
3
50 µm
B
0 min
3.6 min
7.1 min
10.7 min
14.2 min
Control - Round 9
1. AP
2. Intermediate
3. Margin
MO1-3
PCNA
20 µm
C
Bi-lobed embryo
Intermediate
AP
Margin
MO1-3
PCNA
50 µm
D
0 min
3.3 min
6.7 min
10 min
13.3 min
Bi-lobed embryo - Round 9
1. AP
2. Intermediate
3. Margin
MO1-3
PCNA
20 µm

Fig. 5: Zygotic transcription is initiated in a patterned manner along the AP-margin axis

(A) Representative maximum intensity projection image showing an animal pole-view of a control Tg(*actb2:rfp-pcna)* embryo injected with MO1-3-Fluorescein in the 9th division round. Cyan, MO1-3-Fluorescein; magenta, nuclei (PCNA). The three insets, each 120 µm X 120 µm in size, demarcate the regions (1, animal pole; 2, intermediate region; 3, margin) whose higher-magnification images are shown in (B) and (D). (B) Zoomed-in views of the insets shown in A. Cyan dots represent nascent *mi430* transcripts detected by MO1-3-Fluorescein (n=4 embryos). (C) A schematic (top) and a representative orthogonal maximum intensity projection image (bottom) of a bi-lobed Tg(*actb2:rfp-pcna)* embryo injected with MO1-3-Fluorescein embryo in the 9th division round. Cyan, MO1-3-Fluorescein; magenta, nuclei (PCNA). (D) Zoomed-in views of the equivalent regions (1, animal pole; 2, intermediate region; 3, margin) demarcated in (A) for a bi-lobed embryo in the 9th division round. Cyan dots represent nascent *mi430* transcripts (n=3 embryos).